Influence of casting defects on the fatigue behavior of cast aluminum AS7G06-T6

Pooja Mu, Yves Nadot, Carole Nadot-Martin, Amaury Chabod, Itziar Serrano-Muñoz, Catherine Verdu

Influence of casting defects on the fatigue behavior of cast aluminum AS7G06-T6

P. Mu [a], Y. Nadot [a,*], C. Nadot-Martin [a], A. Chabod [b], I. Serrano-Munoz [c], C. Verdu [c]

[a]Institut Pprime, CNRS, ISAE-ENSMA, Université de pahers, Département Physique et Mécanique des Matériaux, 1 Avenue Clément Ader, Futuroscope, France
[b]CTIF, 44 Avenue de la Division Leclerc, Sevres, France
[c]MATEIS, INSA Lyon, Université de Lyon, CNRS, Villeurbanne, France

AS7G06-T6 cast aluminum alloy is tested under tension fatigue loading for two load ratios. After the quantification of the Secondary Dendrite Arm Spacing (SDAS) and grain size of the material, fatigue tests are analyzed through fractographic Scanning Electron Microscope (SEM) observations in order to reveal the type of defects at the origin of the failure. The quantification of the defect size is performed for each defect and Kitagawa type diagrams are produced for each load ratio. It is shown that the critical defect size that does not lower the fatigue strength is close to the grain size of the material. The Defect Stress Gradient (DSG) approach that aims to simulate defect influence on the fatigue strength is presented in a multiaxial context. DSG approach is finally implemented in a finite element simulation of a structural component in order to show that such an approach can provide a defect size map. The latter can be used to define allowable defect size for industrial components.

1. Introduction

The fatigue design of a metallic cast part is strongly linked to the casting process. The designer needs to compromise between the fatigue resistance of the component and the allowable defect size due to the process. In order to perform this optimization, a criterion that takes into account defect influence on the fatigue strength is necessary. Murakami [1] proposed an empirical approach where the defect is measured in relation with loading direction with the so called 'area' defect parameter. This approach can be applied for different defect morphologies and gives interesting results for steels. The designer needs a general methodology that can be applied on a real component in order to evaluate quantitatively the defect size at each point of the component for a given stress and fatigue life. The objective of this paper is to present the Defect Stress Gradient (DSG) method applied to cast aluminum parts in order to show that such methodology can strongly help to define the defect size map on structural components.

Many approaches have been proposed in order to assess the influence of a defect on the fatigue life. An overview of that problem can be found in [2]. The influence of a defect on fatigue life can be determined by 4 parameters:

- Defect type (inclusion, pore, shrinkage, oxide...).
- Defect morphology (spherical, elliptical, complex ...).
- Defect position (internal, sub surface or surface).
- Defect size (function, or not, of loading direction).

For cast parts, defects are typically from few microns to 1–2 mm long so that the microstructure surrounding the defect is of the same order that the defect size because cast microstructure is generally rough. Some authors tended to propose modeling using a microstructural modeling [3] and short crack arrest theories. This approach is relatively limited to uniaxial tension and also in term of R ratio effect due to the use of fracture mechanics. McDowell and coworkers [4] suggested considering 3 scales around the defect in order to describe microstructural influence close to the defect, short crack and finally long crack. This approach using a probabilistic framework is extremely powerful and very realistic from a physical viewpoint. However, it needs a large and reliable experimental data base on fatigue behavior and a good knowledge on fatigue mechanisms for the identification of all parameters. Related to the morphology of the defect, the full 3D analysis of Buffière et al. [5] aims to understand the role of complex local geometry of the defect related to the microstructure. The analysis proposed by Nicoletto et al. [6] adds important information to the 3D damage analysis obtained by X-ray tomography (XR): the variation of stress concentration factor as a function of complex

* Corresponding author. Tel.: +33 5 49 49 80 43; fax: +33 5 49 49 82 38.
E-mail address: yves.nadot@ensma.fr (Y. Nadot).

Nomenclature

a	radius of the spherical inclusion, m
b	material parameter describing the type of defect and its influence in Defect Stress Gradient (DSG) approach, m
h	shortest distance between the specimen free surface and the defect edge, m
f_i	grain area percentage of grains within a certain grain size range
k^P_{avg}	amplifier of mean stress at point P
k^P_{amp}	amplifier of stress amplitude at point P
m	number of summits of a polygon surrounding a defect
$p_i (i = 1, 2, \ldots, m)$	summits of a polygon surrounding a defect
pt	point on defect surface
t	time, s
x_i	coordinates of the point in the matrix, m
(x_i, y_i)	summits coordinates of a polygon surrounding a defect, (m, m)
I	ellipsoidal inhomogeneity
$I_1(\vec{x})$	mathematical function involved in $\overline{\overline{\overline{D}}}(\vec{x})$
$I_2(\vec{x})$	mathematical function involved in $\overline{\overline{\overline{D}}}(\vec{x})$, m^{-2}
J_1	first invariant of the stress tensor, MPa
$J_{1,max}$	maximum value of the first invariant of the stress tensor over a loading cycle, MPa
J^P_1	first invariant of the stress tensor at point P, MPa
$J_{2,a}$	amplitude of the second invariant of the deviatoric stress tensor over a loading cycle, MPa^2
P	point material or crack initiation site
R	load ratio between minimum and maximum stresses of the loading cycle
$R_{p0.2}$	yield strength at 0.2% plastic deformation, MPa
R_m	tensile strength, MPa
S^Γ	area of the polygon Γ, m^2
T	loading period, s
α	material parameter in the Crossland equivalent stress
β	material parameter for a given number of cycles N in Crossland criterion, MPa
δ_{ij}	Kronecker symbol
ν	Poisson's ratio
ν^0	Poisson's ratio of the matrix
σ^∞_{11}	only non-zero component applied at infinity, MPa
σ_a	stress amplitude, MPa
σ_{CR}	Crossland equivalent stress, MPa
$\sigma_{CR,max}$	maximum Crossland equivalent stress on the defect surface, MPa
σ^{pt}_{CR}	Crossland equivalent stress for a point on the defect surface
σ^P_{CR}	Crossland equivalent stress at point P, MPa
σ^∞_{CR}	Crossland equivalent stress at infinity, MPa
σ_D	fatigue strength corresponding to 5×10^6 cycles, MPa
σ^{te}_{D-1}	fatigue strength in tension with the load ratio $R = -1$, MPa
σ_{D0}	previous stress amplitude at which the specimen passed 5×10^6 cycles, MPa
$\sigma^{te}_{D0.1}$	fatigue strength in tension with the load ratio $R = 0.1$, MPa
$\sigma_{eq,max}$	maximum equivalent stress at the defect surface, MPa
σ^∞_{eq}	equivalent stress at infinity, MPa
σ^*_{eq}	equivalent stress including 'gradient' effect in DSG criterion, MPa
σ_{max}	maximum stress
$\sigma^{P_*}_{11}, \sigma^{P_*}_{22}, \sigma^{P_*}_{33}$	components of the stress tensor at point P in the principal coordinate system, MPa
σ^P_{ij}	component of the stress tensor at point P corresponding to a unit load, MPa
ω	angular velocity, s^{-1}
$\Delta\sigma$	variation of stress amplitude between two steps in the "step loading" procedure, MPa
Γ	polygon
Φ	grain size, m
Φ_i	average grain size of grains within a certain grain size range, m
Φ_{avg}	average grain size in the observation zone, m
Ω	infinite matrix
$\vec{u}$	displacement vector, m
$\vec{x}$	vector position of a point in the matrix, m
$\overline{\overline{\overline{\overline{C}}}}^0$	stiffness tensor of the matrix, MPa
$\overline{\overline{\overline{\overline{C}}}}^I$	stiffness tensor of the inhomogeneity, MPa
$\overline{\overline{\overline{\overline{D}}}}(\vec{x})$	fourth-order tensor at point x in the matrix
$\overline{\overline{\overline{\overline{I}}}}$	fourth-order identity tensor
$\overline{\overline{\overline{\overline{P}}}}$	Hill fourth-order tensor $(MPa)^{-1}$
$\overline{\overline{S}}$	deviatoric stress tensor, MPa
$\overline{\overline{S}}^{P_*}$	Deviatoric stress tensor at point P (principal coordinate system), MPa
$\overline{\overline{\overline{\overline{S}}}}$	Eshelby fourth-order tensor
$\overline{\overline{\varepsilon}}$	strain tensor
$\overline{\overline{\varepsilon}}^0$	strain tensor in the matrix at infinity
$\overline{\overline{\varepsilon}}^*$	fictitious equivalent eigenstrain
$\overline{\overline{\varepsilon}}^I$	strain tensor in the inhomogeneity
$\overline{\overline{\sigma}}$	stress tensor, MPa
$\overline{\overline{\sigma}}^0$	stress tensor in the matrix at infinity, MPa
$\overline{\overline{\sigma}}_{loc,max}$	stress tensor at the most loaded point on the spherical void surface, MPa
$\overline{\overline{\sigma}}^{pt}$	stress tensor at each point on the defect surface (side matrix), MPa
$\overline{\overline{\sigma}}^P$	stress tensor at point P, MPa
$\overline{\overline{\sigma}}^P_{g.c.}$	stress tensor at point P in the geometric coordinate system, MPa
$\sqrt{area}$	Murakami parameter describing defect size, square root of the defect surface projected on a plane perpendicular to the direction of the maximum principal stress, m

shrinkage geometry and loading. Therefore, a criterion based on local stresses gets realistic.

From a mechanical point of view, several approaches are summarized as follows. The Critical Distance Method proposed by Susmel and Taylor [7] to describe notch effect on fatigue leads to very good results in the case of small defects as shown by Leopold and Nadot [8]. More recently Pommier and coworkers [9] suggested, in the framework of enriched fracture mechanics, that the T stress could be a way to make a continuous link between small defects and large defects on a Kitagawa type diagram [10]. Other empirical approaches based on Murakami's proposal try to extend the area parameter to multiaxial loading [11].

In order to assess the fatigue life of a part submitted to multiaxial loading, we have proposed a general methodology in the past [12,13,8] to represent the effect of a defect by the stress gradient surrounding the defect like suggested by Papadopoulos [14] or Morel et al. [15]. This general methodology, called Defect Stress Gradient (DSG), can consider explicitly the type, the morphology and the size of the defect. A finite element (FE) submodel is introduced to describe directly the defect at the mesoscopic scale [16].

The DSG approach gives very good results [8,17] for defects ranging from 100 μm to 1 mm but it is limited for application to full scale components by the use of the local FE submodel. To face this problem, an analytical submodel based on the Eshelby's theory is here employed to compute stresses around the defect. The paper addresses the following points:

- Microstructure of the cast Aluminum alloy AS7G06-T6.
- Influence of natural and artificial defects on the fatigue strength under tension for two load ratios (Kitagawa type diagrams).
- Defect Stress Gradient approach, with Eshelby submodel, for an equivalent spherical defect.
- Implementation of the DSG approach as a post treatment of FE numerical analysis of a real industrial part in order to illustrate the capabilities of the DSG criterion to define the defect size map on the part.

2. Material

The material is a cast aluminum alloy AS7G06-T6. Its chemical composition is given in Table 1.

Fig. 1 shows the microstructure of the bulk material, located on the cross section of fatigue samples. Electron Backscatter Diffraction (EBSD) measurements were performed on the specimen surface. EBSD scans were performed in beam control mode with a spatial resolution of 5 μm/step. An area ($6.0 \times 5.0\ mm^2$) was scanned in EBSD measurement, and contained 1449 grains. The grain size (diameter Φ of a disk having the same area as the grain) varies from 28 to 1305 μm. The average grain size is 259 μm, with a standard deviation of 215 μm. The distribution of grain area percentage for different grain sizes is also shown. The total area of the grains within each grain size class is cumulated and divided by the total grain area in the observation zone. It can be seen that the grains between 500 and 600 μm occupy 17.4% of the total area, and the grains in the class $\Phi \in$ [300,800 μm] occupy about ¾ of the total grain area. The average grain size considering the grain size percentage can be calculated below:

$$\Phi_{avg} = \sum_i \Phi_i \cdot f_i \quad (1)$$

where Φ_i is the average grain size of grains within a certain grain size class and f_i is the corresponding grain area percentage. The average grain size considering grain area percentage is 573 μm. The grain size may play an important role in fatigue mechanisms. Indeed, the grain boundaries may act as natural barriers of crack propagation and thus, an additional energy is required to propagate the crack from one grain to another [18,19].

The observation by optical microscope reveals the microstructure of the material at a smaller scale. A dendritic structure is observed (solid solution primary α and eutectic Al–Si surrounding), as seen in Fig. 2a. Shrinkage cavities can also be seen in Fig. 2a. Fig. 2b shows the measurement of the Secondary Dendrite Arm Spacing (SDAS). The measurement was done by dividing the distance of several secondary dendrite arms by the total number of arms. Only the dendrites with at least 6 arms have been used in the measurement in order to reduce the measurement error. 155 dendrites were measured and the distribution of SDAS is shown in Fig. 3. The SDAS varies between 26 and 57 μm, following a normal distribution. 3/4 of the SDASes are located in the range [31,43 μm]. The average SDAS is 38 μm, with a standard deviation of 6 μm.

Table 1
Composition of the AS7G06-T6 used in this study (wt.%).

Si	Mg	Fe	Cu	Mn	Ni	Zn	Pb	Sn	Ti
7.00	0.56	0.097	<0.015	<0.03	<0.01	<0.01	<0.003	<0.01	0.13

3. Experimental procedure and results

3.1. Preparation of materials and specimens

As for the casting procedure, the cast aluminum alloy AS7G06 T6 was obtained by gravity die casting. 95 kg 100% new ingots were cast in each casting, which correspond to 40 specimens. An electric furnace was used. The casting temperature was 720 °C+/−10 °C and the mold temperature was 350 °C when closing die. Opening and shake-out lasted 120 s after filling. Hydrogen degassing and oxide removing were done by argon injection into aluminum bath (5–7 l/min during 7 min, before and after composition corrections) with 0.1% deoxidation flux COVERAL GR 2410 and a 0.05% degassing flux.

Besides composition, the temperature, porosity (fraction of the volume of voids over the total volume of the casting) and density (mass per unit volume of the casting) were also controlled during casting.

The thermal treatments in the T6 condition were: heating to solution at 540 °C for 10 h, quenching in cold water, aging at room temperature for 24 h, and then aging at 160 °C for 8 h.

The material was supplied as cast as a bar of 270 mm length and 30 mm diameter (Fig. 4). Two cylindrical specimens were machined off the bar, following the sketch given in Fig. 4.

3.2. Nondestructive testing

The specimens were observed by Non Nondestructive Testing (NDT): XR and Dye Penetrant Liquid. The numerical X-ray detection has been done using the specification NF EN 12681 and the equipment Tube Yxlon Y.TU/320-D03. The detecting thickness was 30 mm. The voltage was 90 kV. The focus-to-film distance was 1 m; the geometric unsharpness was 0.15 mm; and the angle of incidence was 90°. The specimen was exposed for 30 s in the intensity 5. The visible Image Quality Indicator (IQI) was W12 (0.25 m) following the specification NF EN 462-1. The Dye Penetrant Liquid detection was done following specifications NF EN 571-1 and NF EN 1371-1. Both visible and ultraviolet lightings were used. The residual of the Dye Penetrant Liquid had an illuminance of 6 lux under UV for visible lighting, and an irradiance of $14\ W/m^2$ for ultraviolet lighting. A fluorescent penetrant of sensibility S2 was adopted. The impregnation time was 20 min and the temperature was 22 °C. The penetrant was later eliminated with water and air, under a pression below 2 bars. After a drying procedure under 45 °C for 3 min, a dry revelator was applied. After 10 min, the specimen was ready for examination. The recording time was controlled to be under 30 min.

7 specimens have been used to analyze the size distribution and the porosity ratio of shrinkage cavities. The pluging Fiji "Labeling 3D" was adopted to identify the size of each cavity in the stack, whereas the pluging "fracz" which ran through each slice of a stack (there are about 2500 slices per stack) was used to analyze the volume fraction of shrinkage cavities. Fig. 5 shows the size distribution of 5088 shrinkage cavities. It can be seen that the pore frequency decreases as its volume increases. Over 2/3 of the analyzed pores are smaller than 200,000 μm^3. As for the porosity ratio, 17,947 slices in 7 stacks were analyzed. The pore ratio in terms of volume fraction is 0.0243.

Samples tested are classified as grade 1 according to ASTM E155 [20], Al alloy, shrinkage cavity, ¼ inch. Samples have therefore a minimum amount of shrinkage. Dye Penetrant can reveal some oxides at the free surface. All samples containing oxides were rejected for fatigue tests, as done for the industrial components.

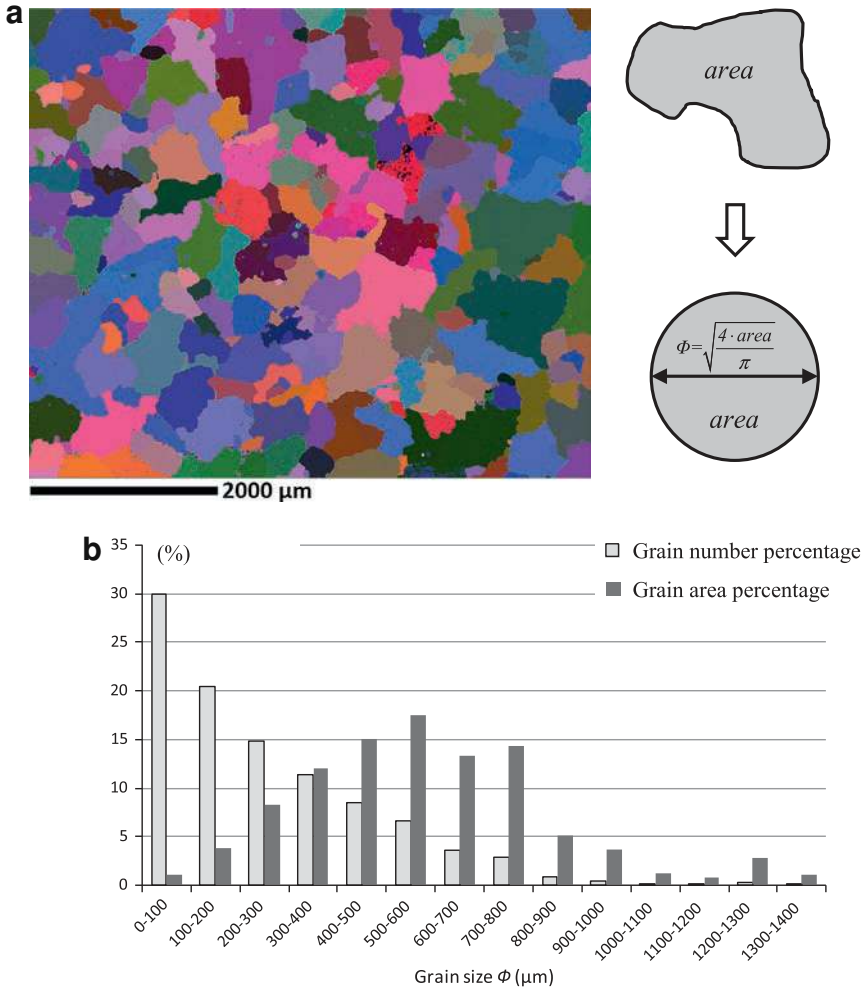

Fig. 1. Grain size of the cast aluminum alloy AS7G06-T6: (a) EBSD micrograph of a zone ($6.0 \times 5.0\ mm^2$) and calculation of the grain size disk; (b) distributions of grain number percentage (1449 grains) and of grain area percentage.

3.3. Tensile test

Monotonic tensile tests were done following the specification NF EN ISO 6892-1 on a machine ZWICK BT1.FR100THW.A2K, whose capacity is 100 kN. 3 cylindrical specimens with a diameter of 10 mm and a useful length of 50 mm were tested. The extensometer ZWICK BTC-EXMACRO.011 has a basic length of 50 mm. Fig. 6 shows the stress–strain curve. The material has a yield strength $R_{p0.2}$ = 275 MPa and a tensile strength R_m = 335 MPa. The linear elastic part was used for the identification of Young's modulus. The identification was made with tensile experimental results for three specimens. The average value of Young's modulus over the three specimens is 73 GPa and the Poisson's ratio v is 0.3.

3.4. Fatigue test

Tension fatigue tests were performed by the means of Amsler vibrophore (electromagnetic resonance machine) under force control using the samples presented in Fig. 4. The test frequency was 108 Hz. The drop of test frequence (5 Hz) was adopted as the stop condition of fatigue tests. When a test is stopped under this condition, the sample is almost broken and contains a macroscopic crack deeper than half diameter of the sample. Fatigue tests were conducted at two load ratios: $R = -1$ and 0.1. Fatigue strengths are given using the stress amplitude defined as the maximum stress minus the mean stress over the load cycle. The fatigue strengths mentioned in the following of the paper correspond to 5×10^6 cycles of fatigue loading. In order to be able to produce Kitagawa type diagrams [10] for different defect sizes and different types of defect, the "step loading" procedure was used to evaluate the fatigue strength of a sample [21]. The fatigue test was started on a sample at a given load for 5×10^6 cycles. If the sample was broken at the initial stress amplitude, the fatigue strength was lower than the applied stress amplitude. Of course this is a deterministic view of the result that does not take into account the scatter. It is therefore possible to have a sample failed below the average fatigue strength. In absence of any failure, it was considered that the corresponding fatigue strength is higher than the recent stress amplitude and the sample was loaded again at a higher stress level. In this study the increase of stress amplitude was 10 MPa. This procedure was repeated until failure. In this case, the fatigue strength can be calculated as below:

$$\sigma_D = \sigma_{D0} + \frac{\Delta\sigma}{2} \tag{2}$$

where σ_{D0} is the previous stress amplitude at which the specimen did not break in 5×10^6 cycles, and $\Delta\sigma$ is the variation of stress amplitude between two steps ($\Delta\sigma$ = 10 MPa here).

Bellows et al. [21] used the procedure on Ti64. It is the only procedure to evaluate the fatigue strength of a sample for a natural defect because it is impossible to generate an S–N curve for a set of samples containing the same defect type, location and size. The

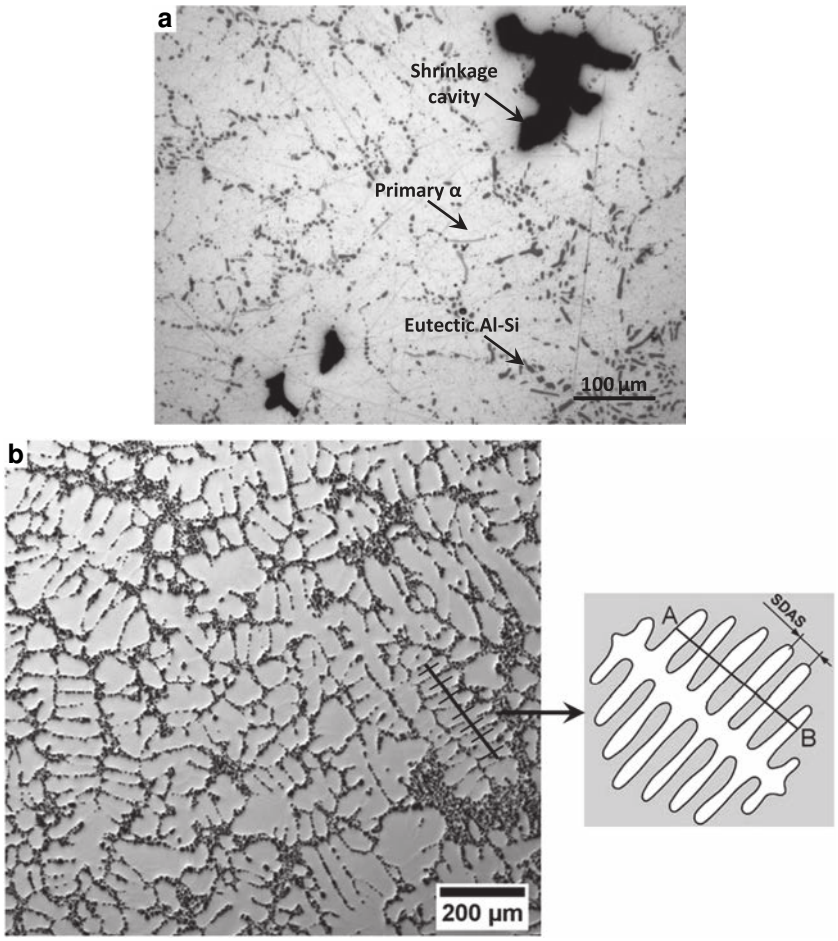

Fig. 2. (a) Microstructure of the cast aluminum alloy AS7G06-T6; (b) measurement of SDAS.

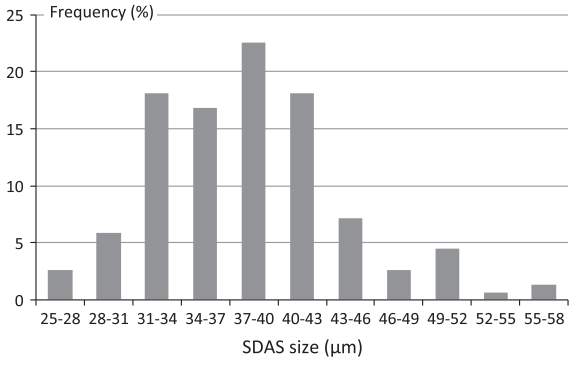

Fig. 3. Distribution of SDAS size (based on 155 measured results).

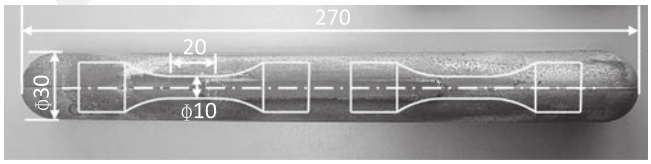

Fig. 4. As cast cylindrical bar and specimen location.

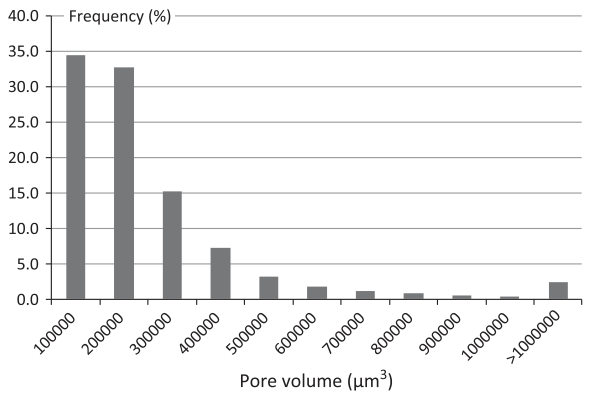

Fig. 5. Size distribution of shrinkage cavities.

analysis of the set of results will inform whether or not the material is sensitive to the famous coaxing effect [22]. For the AS7G06-T6 tested, there is no evidence of the effect of loading history. It seems therefore that the step loading is appropriate to make an estimation of the fatigue strength using one sample.

As presented in the literature [5,23–25], the aluminum alloys have no evident fatigue limit. So we use the Basquin's law to moderate the Wöhler curves in Fig. 7. The least square approximation was used to fit the Wöhler curve to the experimental points. 15 and 10 experimental points were used for fitting the Wöhler curve for the load ratio $R = -1$ and 0.1, respectively. Results obtained in Fig. 7 are supposed to be "defect free" in the sense of an industrial classification: class 1 ASTM E155 Al alloy, shrinkage cavity, ¼ inch

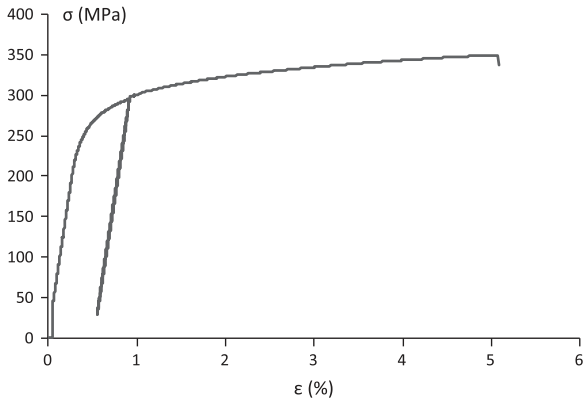

Fig. 6. Stress–strain curve for the cast aluminum alloy AS7G06-T6.

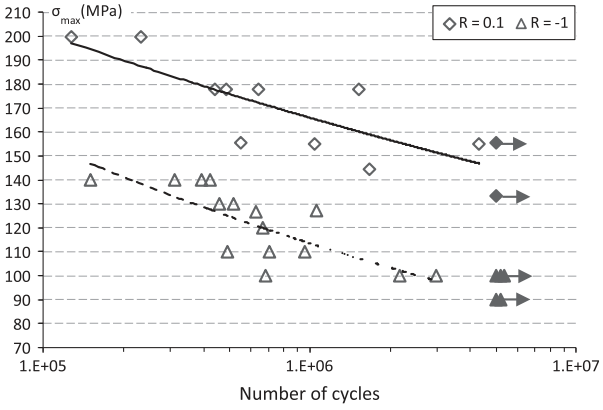

Fig. 7. Wöhler curves for the cast aluminum alloy AS7G06-T6 with two different load ratios.

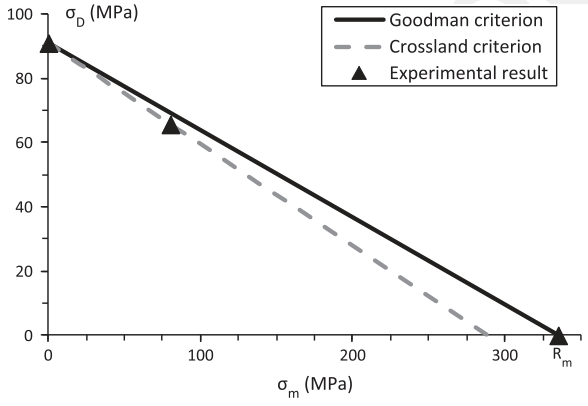

Fig. 8. Haigh diagram for the cast aluminum alloy AS7G06-T6.

plus Dye Penetrant surface examination. They will be used in the following as the reference "defect free" material on the Kitagawa diagram to study the influence of the defect. These results are in agreement with results in the literature on very similar materials [5,26–29].

Before analyzing the fracture surface, it is interesting to study the mean stress effect on this material. For this purpose, the Haigh diagram is plotted in Fig. 8 where the evolution of the fatigue strength is plotted against the mean stress. It is interesting to remark that the mean stress effect can be described by Goodman approach, as suggested by Sonsino and Grubisic [30]. Recent results

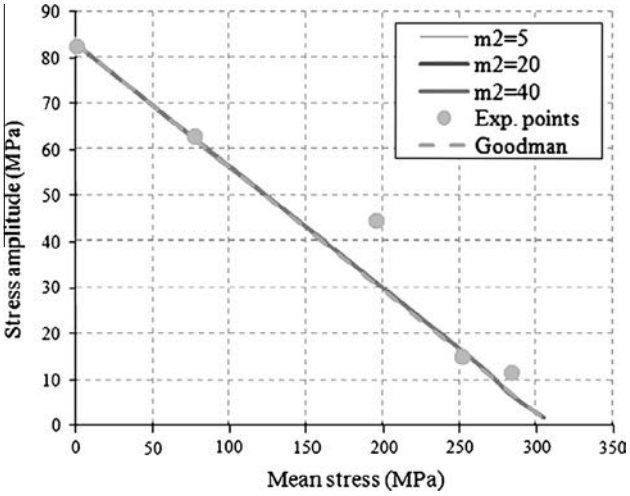

Fig. 9. Haigh diagram for alloy Al7SiCu05Mg03 (Plane Bending) [29].

obtained by Koutiri et al. [28,29] confirm this behavior. Fig. 9 shows the Haigh diagram proposed by Koutiri et al. [28,29] for an alloy Al7SiCu05Mg03, very close to the material AS7G06-T6. The experimental data based on different load ratios (from 0 to 0.92) have been shown. The stress amplitude decreases linearly as the mean stress increases, following the Goodman's law. In the following, a multiaxial criterion will be used to describe the influence of a defect on the fatigue behavior. It is interesting to note that the Crossland criterion [31], identified using two fatigue strengths ($\sigma^{te}_{D-1} = 91$ MPa, $\sigma^{te}_{D0.1} = 66$ MPa for $N = 5 \times 10^6$), has a very similar behavior to Goodman's straight line (Fig. 8). It is therefore a good approximation to use Goodman approach to determine the mean stress sensitivity of the cast aluminum alloy. Therefore, when no other experimental data is available, we only need to know σ^{te}_{D-1} and R_m as material parameters.

3.5. Analyze of fracture surface

In order to identify the crack initiation sites, the fracture surface has been observed after failure. Fig. 10a shows a characteristic fracture surface viewed by optical microscope. Three parts can be distinguished: a crack initiation site marked by *P* where all the propagation rivers converge; a bright zone 1 around the crack initiation site which corresponds to the stable fatigue crack propagation phase; a ductile zone 2 far from the crack initiation site which corresponds to the final ductile fracture. The feature of the crack initiation site *P* can be very different from a sample to another as mentioned by [32]. It could be:

- A crystallographic initiation without defect, probably in the primary α phase from a crystallographically well orientated slip system in a surface grain (Fig. 10b).
- A shrinkage cavity (Fig. 10c).
- An oxidized skin (Fig. 10d and e). Fig. 10e indicates that the defect zone in Fig. 10d had a different chemical composition from that of the matrix. This defect has an appearance of an oxidized skin. The oxidized defect in Fig. 10d and e was formed during casting process. It was not revealed by the dye penetrant non destructive examination because it is a subsurface defect.

3.6. Defect size measurement and Kitagawa diagram

In this study, the parameter $\sqrt{area}$ proposed by Yukitaka Murakami [1] was adopted to calculate the defect size. $\sqrt{area}$ is the

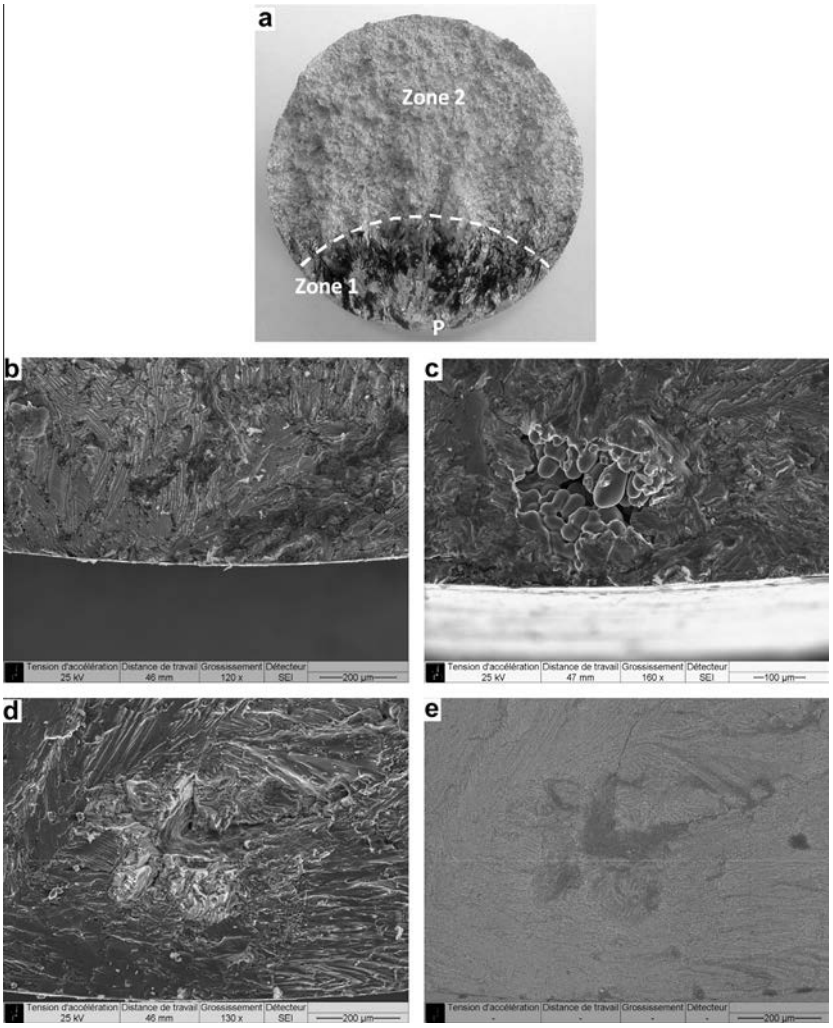

Fig. 10. (a) General specimen fracture surface (optical microscope); (b) initiation from primary α (SEM); (c) shrinkage cavity (SEM); (d) oxide (SEM); (e) oxide (SEM, Backscattered Electrons).

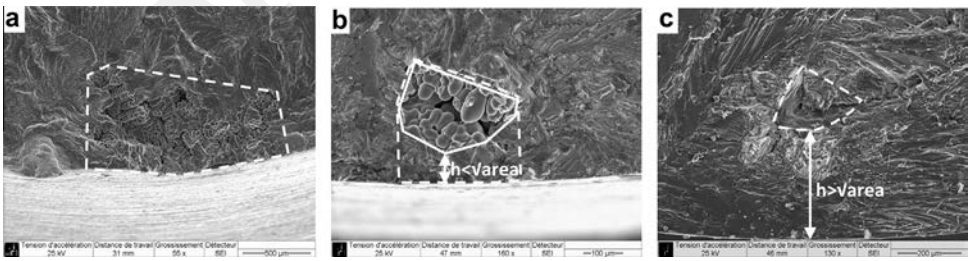

Fig. 11. Measurement of defect size. (a) surface defect; (b) defect close to the free surface; (c) defect far from the free surface.

square root of the defect surface projected on a plane perpendicular to the direction of maximum principal stress. For a defect with an irregular shape, for example the defect shown in Fig. 10d and e, it is important to develop a method to measure the size. Moreover, the position of a defect relative to the specimen surface varies. The calculation of the defect size should consider this parameter, too. As shown in Fig. 11a, for a surface defect, we enclose the defect with a polygon. The area of the contour can be calculated and then the parameter $\sqrt{area}$ can be derived. For the cases of Fig. 11b and c, we first calculated $\sqrt{area}$ by surrounding the defect with a polygon. Then the parameter $\sqrt{area}$ was compared to the shortest distance between the specimen free surface and the defect edge, noted h in Fig. 11b and c. If $h < \sqrt{area}$ (case of Fig. 11b), the ligament between the defect and the specimen free surface is very weak because of the stress concentration and has to be considered in the calculation of $\sqrt{area}$. So a new polygon surrounding the defect and the ligament was defined to calculate the new parameter $\sqrt{area}$. If $h > \sqrt{area}$ (case of Fig. 11c), the defect was considered as an isolated internal defect and the ligament was not taken into account in the calculation of $\sqrt{area}$. This way to separate surface and internal defects is also supported by [33].

The analytical method due to [34] was adopted to calculate the area of a polygon from the coordinates of its summits. The area of the polygon Γ with m summits p_i ($i = 1, 2, \ldots, m$) whose coordinates are noted (x_i, y_i), is given by [34]:

$$S^{\Gamma} = \frac{1}{2}\sum_{i=1}^{m}(x_i \cdot y_{i+1} - x_{i+1} \cdot y_i) \quad (3)$$

with $x_{m+1} = x_1$, $y_{m+1} = y_1$.

All the fracture surfaces were observed and it was not possible to make any correlation between fatigue life and defect size in Fig. 7. The defect population in the samples tested to build the Wöhler curves in Fig. 7 is therefore the one that can be encountered in the defect free material, with no impact on the fatigue strength nor on fatigue life. It seems that another parameter governs the fatigue life for this defect population. It could be crystallographic grain size as suggested by [26,27]. Samples broke from primary α Al, shrinkage or internal oxides.

The samples with small internal defects of grade 1 according to the standard reference radiographs ASTM E155 are considered "defect free" in this study. As we will see it in Fig. 13, small defects have no influence on the fatigue strength. Therefore, in order to study the evolution of the fatigue strength with defect size, bigger surface defects were machined. Artificial defects were produced using the spark erosion machining principle method, as shown in Fig. 12. A copper wire carrying a current generates a high intensity electric arc that melts the material locally and machines desired default. To obtain a semi-spherical defect, the defect depth is equal to the diameter of the wire, as shown in Fig. 12a. Fig. 12b shows the fracture surface of a specimen with an artificial defect located at the specimen surface. The shape of the defect can be seen.

Figs. 13 and 14 present the Kitagawa diagrams for the alloy AS7G06-T6 with load ratios $R = -1$ and 0.1. The solid symbols correspond to specimens that did not break in 5×10^6 cycles at each loading step, and the hollow symbols correspond to specimens that broke during 5×10^6 cycles at the last loading step. The experimental points in Fig. 13 can be divided into 3 groups according to defect types. The specimens in zone A had no defect (Fig. 10b).

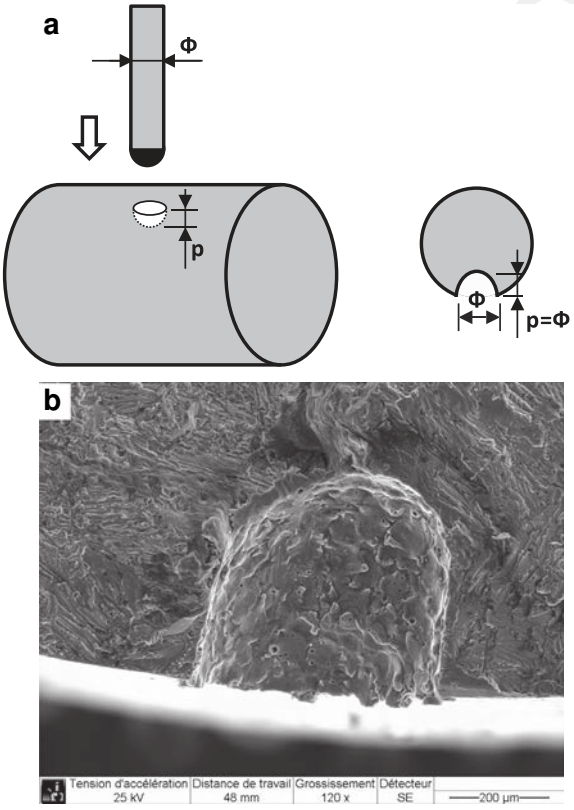

Fig. 12. Artificial defect: (a) spark erosion machining principle; (b) artificial defect on the specimen after fracture (SEM).

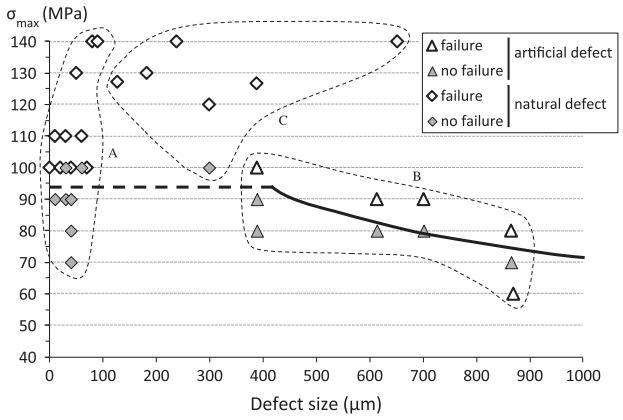

Fig. 13. Kitagawa diagram for the cast aluminum alloy AS7G06-T6. Tension loading, $R = -1$.

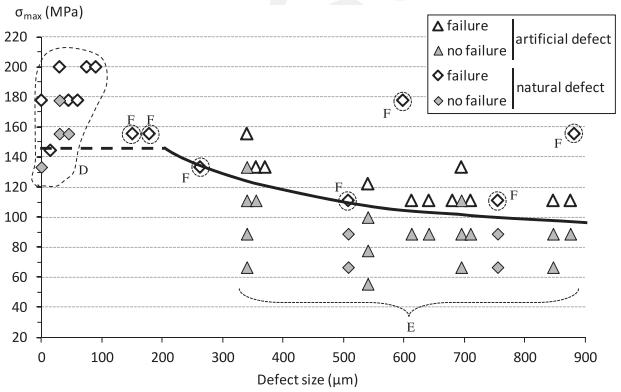

Fig. 14. Kitagawa diagram for the cast aluminum alloy AS7G06-T6. Tension loading, $R = 0.1$.

The defect sizes for the zone A shown in Fig. 13 aim only at separating the results from different specimens for clarity purpose. The points in zone B correspond to specimens with artificial defects (Fig. 12) having relatively large sizes between 388 and 865 µm. These points are essential to the Kitagawa diagram, as the defect influence can be seen only when the defect is big enough. The points in zone C correspond to specimens with shrinkage cavities (Fig. 10c) whose sizes vary from 127 to 651 µm. Most of them are internal or subsurface defects. It is reminded that the "step loadings" method has been applied. If a specimen was not broken after 5×10^6 cycles, an increment of stress amplitude of 10 MPa was applied on the same specimen. Only one of the specimens with shrinkage cavities was broken at the second loading step. This result shows that the fatigue strength is not lowered by a subsurface shrinkage cavity of 300 µm.

Fig. 14 shows the Kitagawa diagram for the load ratio $R = 0.1$. The maximum defect size is 882 µm. The fatigue strength is lowered when the defect size is larger than 200 µm. Zone D (respectively E) shows the points for specimens without defect (Fig. 10b) (respectively artificial defects (Fig. 12)). Fracture surfaces with a crack initiated from shrinkage cavity (Fig. 10c) are found for specimens in zone F. The shrinkage size varies between 151 and 882 µm. It seems that this material is not sensitive to defect type because a shrinkage of given size gives similar results compared to an artificial defect of the same size.

From these results, it was found that the defect decreased the fatigue strength only when its size exceeded a critical size of 400 µm and 200 µm for $R = -1$ and 0.1, respectively. This value has the same order of magnitude as the grain size (259–573 µm)

but is really bigger than the SDAS (38 μm). Further analysis should be done to fully understand the influence of microstructure on the critical defect size. The shrinkage cavities (smaller than 300 μm) have no influence on the fatigue strength. The evolution of the fatigue strength with the defect size is estimated and presented by solid lines in Figs. 13 and 14. The dotted lines correspond to the fatigue strength obtained on the defect free material presented before.

4. Procedure and results of numerical simulation

Several approaches can be used to simulate the Kitagawa diagram. The LEFM (Linear Elastic Fracture Mechanics) criterion considers a defect as an initial crack. Murakami uses an empirical criterion based on the Vickers hardness, load ratio and defect size [35]. The CDM (Critical Distance Method) criterion is based on measurement of a criterion at a given distance from the surface [7] (Fig. 15). The DSG (Defect Stress Gradient) criterion is based on the stress gradient around the defect [13,16] (Fig. 15).

Simulation results obtained with the above mentioned criteria were compared previously with experimental results in tension, torsion and tension–torsion with a load ratio of −1 for A356-T6 aluminum [17]. It may be noted that the LEFM and Murakami criteria give conservative and non-conservative results, with an average error of 19% and 20% respectively. The CDM and DSG criteria give more accurate conservative results, with an average error of 11% and 9%. So the CDM and DSG criteria are more suitable for simulation, but they need more physical parameters [17].

The LEFM criterion and the Murakami criterion give direct relationship between stress and defect size. These two criteria do not request the calculation of stresses around a defect. However, the CDM and DSG criteria first analyze the stresses around the defect through FE analysis or analytical method using the Eshelby theory (which will be introduced in Section 4.2), then calculate the equivalent stress. The equivalent stress for multiaxial stresses can be calculated based on several criteria, for example, the simple criteria proposed by Crossland [31], Dang Van et al. [36], or the principal stress criterion. In this study, the DSG criterion using the Crossland criterion for calculating the fatigue equivalent stress is adopted and will be presented in the following paragraph. For more complex loads (out of phase), it is preferable to use the criterion of Vu et al. [37].

4.1. Defect Stress Gradient (DSG) criterion

The Defect Stress Gradient (DSG) criterion, proposed by Nadot and Billaudeau [13] and improved by Gadouini et al. [16], can be used for materials with surface defects. It is based on the formulation of Crossland and employs a stress 'gradient' around a defect to describe the defect influence on the fatigue strength.

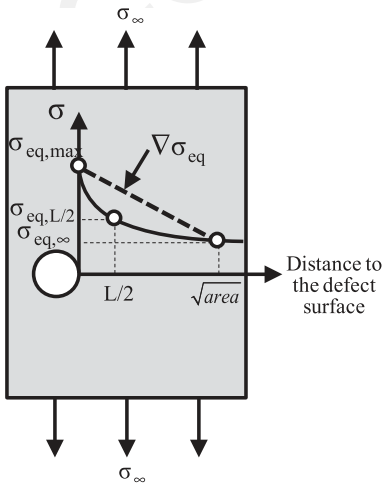

Fig. 15. Principle of CDM and DSG criteria.

The DSG criterion may be written as follows:

$$\sigma^*_{eq} = \sigma_{eq,max} - b \cdot \frac{\sigma_{eq,max} - \sigma^{\infty}_{eq}}{\sqrt{area}} = \beta \tag{4}$$

where σ^*_{eq} is the DSG equivalent stress including 'gradient' effect, $\sigma_{eq,max}$ is the maximum equivalent stress at the defect surface, σ^{∞}_{eq} is the equivalent stress far from the defect, $\sqrt{area}$ is the defect size, b is a material parameter and β is a material parameter for a given number of cycles N.

The equivalent stresses $\sigma_{eq,max}$ and σ^{∞}_{eq} involved in Eq. (4) can be calculated using the criterion that is appropriate to describe the multiaxial fatigue behavior of the defect free material. The DSG methodology is indeed independent on the criterion [38]. In this study, Crossland criterion [31] is adopted. The Crossland equivalent stress is a linear combination of the amplitude of the second invariant of the deviatoric stress tensor $J_{2,a}$ and the maximum hydrostatic stress $J_{1,max}$ over a loading cycle.

$$\sigma_{CR} = \sqrt{J_{2,a}} + \alpha \cdot J_{1,max} \tag{5}$$

Using the Crossland equivalent stress, σ^*_{eq} in Eq. (4) becomes:

$$\sigma^*_{eq} = \sigma_{CR,max} - b \cdot \frac{\sigma_{CR,max} - \sigma^{\infty}_{CR}}{\sqrt{area}} \tag{6}$$

with $\sigma_{CR,max}$ the maximum Crossland equivalent stress on the defect surface and σ^{∞}_{CR} the Crossland equivalent stress far from the defect.

The calculation of $J_{2,a}$ may be done as follows [39]:

$$J_{2,a} = \frac{1}{2\sqrt{2}} \max_{t_i \in T} \left\{ \max_{t_j \in T} \sqrt{\left(\overline{\overline{S}}(t_i) - \overline{\overline{S}}(t_j)\right) : \left(\overline{\overline{S}}(t_i) - \overline{\overline{S}}(t_j)\right)} \right\} \tag{7}$$

with $\overline{\overline{S}}$ the deviatoric stress tensor.

The value of $J_{2,a}$ is obtained by a double maximization over the loading period T. To avoid heavy computation and to be close to experiments, only proportional and sinusoidal loadings have been here considered, and the calculations limited within the elastic range. In this case, the stress tensor at a point P of a model is (in the geometric coordinate system):

$$\overline{\overline{\sigma}}^{P}_{g.c.} = \begin{pmatrix} \sigma^P_{11} & \sigma^P_{12} & \sigma^P_{13} \\ \sigma^P_{12} & \sigma^P_{22} & \sigma^P_{23} \\ \sigma^P_{13} & \sigma^P_{23} & \sigma^P_{33} \end{pmatrix} \left(k^P_{avg} + k^P_{amp} \cdot \sin \omega t \right) \tag{8}$$

where σ^P_{ij} is the component of the stress tensor at point P corresponding to a unit load. k^P_{avg} and k^P_{amp} are the amplifiers of the mean stress and the stress amplitude, ω is the angular frequency and t is the time. The stress tensor is transferred from geometric coordinate system to the principal coordinate system in order to facilitate its further application at the scale of the defect. In the principal coordinate system, there are only three nonzero components $\sigma^{P^*}_{11}$, $\sigma^{P^*}_{22}$, $\sigma^{P^*}_{33}$.

For a load with an angular frequency $\omega = 2\pi\ s^{-1}$ and the loading period $T = 1$ s, each component of the deviatoric stress in the principal coordinate system reaches its maximum (or minimum) value when $t = 0.25$ s (or $\omega t = \pi/2$), and minimum (or maximum) value when $t = 0.75$ s (or $\omega t = 3\pi/2$). Thus, for a proportional sinusoidal load and if the calculation is limited in elasticity, Eq. (7) can be simplified as follows:

$$J_{2,a} = \frac{1}{2\sqrt{2}} \sqrt{\left(\overline{\overline{S}}^{P*}\left(\frac{T}{4}\right) - \overline{\overline{S}}^{P*}\left(\frac{3T}{4}\right)\right) : \left(\overline{\overline{S}}^{P*}\left(\frac{T}{4}\right) - \overline{\overline{S}}^{P*}\left(\frac{3T}{4}\right)\right)} \tag{9}$$

The first stress invariant at point P, J^P_1, can be written:

$$J_1^P = \frac{\sigma_{11}^{P^*} + \sigma_{22}^{P^*} + \sigma_{33}^{P^*}}{3}\left(k_{avg}^P + k_{amp}^P \cdot \sin \omega t\right) \tag{10}$$

J_1^P also varies sinusoidally. It reaches its maximum value when $t = T/4$ or $3T/4$. So we can store the values for these two instants and compare them to obtain $J_{1,max}$:

$$J_{1,max} = max\left(J_1^P\left(\frac{T}{4}\right), J_1^P\left(\frac{3T}{4}\right)\right) \tag{11}$$

The DSG criterion needs both the global stresses far from the defect and on the defect surface. In order to calculate the local stresses when a load is applied (uniformely) away from the defect, the Eshelby's approach is used. It is introduced in the next section.

4.2. Analytical computation of stresses using Eshelby's method

This section is focused on the analytical Eshelby's approach [40,41], proposed here as an alternative to the FEM in order to compute the stress field around a defect. First, the general theoretical basis of the approach is briefly reminded. Then, closed-form equations, useful for practical application in the DSG framework in the particular case of a spherical defect, are given. They have been programmed in Fortran 90 and finally incorporated into an UVARM for ABAQUS®.

The size of the defect is supposed to be small compared to the size of the material volume surrounding it. In other words, the defect is considered as isolated in an infinitely extended medium submitted to an applied stress tensor $\overline{\overline{\sigma}}^0$ at infinity.

4.2.1. Theoretical basis of the approach

For generality purpose, we consider an isolated ellipsoidal inhomogeneity I, with constant elasticity tensor $\overline{\overline{\overline{\overline{C}}}}^I$, embedded in an infinite medium Ω (the matrix) with a different elasticity tensor $\overline{\overline{\overline{\overline{C}}}}^0$, subjected to a uniform strain tensor $\overline{\overline{\varepsilon}}^0$ at infinity (corresponding stress tensor $\overline{\overline{\sigma}}^0$). The aim is to investigate the disturbance caused by the presence of the inhomogeneity. The governing equations of this problem are precisely the same as those presented in Eshelby's elastic inhomogeneity problem [41]:

$$\begin{cases} \overrightarrow{div}\ \overline{\overline{\sigma}} = \vec{0} \\ \overline{\overline{\sigma}} = \overline{\overline{\overline{\overline{C}}}}^I : \overline{\overline{\varepsilon}} \quad in\ I \\ \overline{\overline{\sigma}} = \overline{\overline{\overline{\overline{C}}}}^0 : \overline{\overline{\varepsilon}} \quad in\ \Omega/I \\ \vec{u} = \overline{\overline{\varepsilon}}^0 \cdot \vec{x} \quad when \quad \|\vec{x}\| \to \infty \end{cases} \tag{12}$$

The inhomogeneity problem (Eq. (12)) is equivalent to the classical Eshelby's homogeneous inclusion problem [40] with uniform strain at infinity:

$$\begin{cases} \overrightarrow{div}\ \overline{\overline{\sigma}} = \vec{0} \\ \overline{\overline{\sigma}} = \overline{\overline{\overline{\overline{C}}}}^0 : (\overline{\overline{\varepsilon}} - \overline{\overline{\varepsilon}}^*) \quad in\ I \\ \overline{\overline{\sigma}} = \overline{\overline{\overline{\overline{C}}}}^0 : \overline{\overline{\varepsilon}} \quad in\ \Omega/I \\ \vec{u} = \overline{\overline{\varepsilon}}^0 \cdot \vec{x} \quad when \quad \|\vec{x}\| \to \infty \end{cases} \tag{13}$$

if a fictitious eigenstrain $\overline{\overline{\varepsilon}}^*$ defined by:

$$-\overline{\overline{\overline{\overline{C}}}}^0 : \overline{\overline{\varepsilon}}^* = \left(\overline{\overline{\overline{\overline{C}}}}^I - \overline{\overline{\overline{\overline{C}}}}^0\right) : \overline{\overline{\varepsilon}}\ in\ I \tag{14}$$

is introduced. The above methodology to formally equate the Eshelby's inhomogeneity and homogeneous inclusion problems, through the introduction of a fictitious, equivalent, eigenstrain $\overline{\overline{\varepsilon}}^*$, is classically called Equivalent Inclusion Method (EIM). This equivalency allows deriving the solution of Eq. (12) from the solution of Eq. (13). Indeed, according to [40], if a uniform eigenstrain $\overline{\overline{\varepsilon}}^*$ (also called stress-free transformation strain) is prescribed in a finite subdomain (inclusion) of an infinitely extended homogeneous medium, the strain in the inclusion, $\overline{\overline{\varepsilon}}^I$, is also uniform and is expressed as a linear function of this eigenstrain:

$$\overline{\overline{\varepsilon}}^I = \overline{\overline{\overline{\overline{S}}}} : \overline{\overline{\varepsilon}}^* + \overline{\overline{\varepsilon}}^0 \tag{15}$$

where $\overline{\overline{\overline{\overline{S}}}}$ is the Eshelby's tensor. The components of $\overline{\overline{\overline{\overline{S}}}}$ are dimensionless and depend on $\overline{\overline{\overline{\overline{C}}}}^0$ and on the geometry of the inclusion (not the size). Therefore, $\overline{\overline{\varepsilon}}^*$ which is here defined by Eq. (14) to ensure the equivalence between problems (Eq. (12) and (13)), is also uniform. Owing to uniqueness of the solution of an elasticity problem, Eshelby's solution of the homogeneous inclusion problem (Eq. (13)), associated to $\overline{\overline{\varepsilon}}^*$ given by Eq. (14), is thus the solution of the inhomogeneity problem (Eq. (12)). This is true for points both inside and outside the inclusion. By using Eq. (15), $\overline{\overline{\varepsilon}}^*$ given by Eq. (14) may be written as a function of the strain tensor at infinity:

$$\overline{\overline{\varepsilon}}^* = -\left(\left(\overline{\overline{\overline{\overline{C}}}}^I - \overline{\overline{\overline{\overline{C}}}}^0\right) : \overline{\overline{\overline{\overline{S}}}} + \overline{\overline{\overline{\overline{C}}}}^0\right)^{-1} : \left(\overline{\overline{\overline{\overline{C}}}}^I - \overline{\overline{\overline{\overline{C}}}}^0\right) : \overline{\overline{\varepsilon}}^0 \tag{16}$$

In the same way, inserting Eq. (14) in Eq. (15) provides the direct expression of $\overline{\overline{\varepsilon}}^I$ as a function of $\overline{\overline{\varepsilon}}^0$:

$$\overline{\overline{\varepsilon}}^I = \left(\overline{\overline{\overline{\overline{I}}}} + \overline{\overline{\overline{\overline{P}}}} : \left(\overline{\overline{\overline{\overline{C}}}}^I - \overline{\overline{\overline{\overline{C}}}}^0\right)\right)^{-1} : \overline{\overline{\varepsilon}}^0 \tag{17}$$

with $\overline{\overline{\overline{\overline{P}}}} = \overline{\overline{\overline{\overline{S}}}} : \overline{\overline{\overline{\overline{C}}}}^{0-1}$ the Hill's tensor [42] and $\overline{\overline{\overline{\overline{I}}}}$ the classical fourth-order tensor defined by $I_{ijkl} = \frac{1}{2}(\delta_{ik} \cdot \delta_{jl} + \delta_{il} \cdot \delta_{jk})$.

When the infinite medium is isotropic, the Eshelby's tensor $\overline{\overline{\overline{\overline{S}}}}$ may be found analytically using for instance the Green function concept. Moreover, the strain field in the matrix is obtained as a linear function of the eigenstrain $\overline{\overline{\varepsilon}}^*$ whatever the geometry of the ellipsoidal inclusion. Below are given the expressions of $\overline{\overline{\overline{\overline{S}}}}$ and of the strain field in the matrix for a spherical inclusion with radius a, and centered at the origin of the Cartesian coordinate system.

4.2.2. Detailed expressions for a sphere

The components of the Eshelby's tensor are (e.g. see [43]):

$$S_{1111} = S_{2222} = S_{3333} = \frac{7 - 5\nu^0}{15(1-\nu^0)},\quad S_{1212} = S_{2323} = S_{3131} = \frac{4 - 5\nu^0}{15(1-\nu^0)},$$
$$S_{1122} = S_{2233} = S_{3311} = S_{1133} = S_{2211} = S_{3322} = \frac{5\nu^0 - 1}{15(1-\nu^0)} \tag{18}$$

where ν^0 is the Poisson's ratio of the matrix.

The strain field $\overline{\overline{\varepsilon}}(\vec{x})$ in the matrix is given by [43]:

$$\overline{\overline{\varepsilon}}(\vec{x}) = \overline{\overline{\overline{\overline{D}}}}(\vec{x}) : \overline{\overline{\varepsilon}}^* + \overline{\overline{\varepsilon}}^0 \tag{19}$$

where $\overline{\overline{\overline{\overline{D}}}}(\vec{x})$ is the fourth-order tensor represented as follows:

$$\begin{aligned} 8\pi(1-\nu^0)D_{ijk\ell} = {} & \delta_{ij} \cdot \delta_{k\ell}[(2\nu^0 - 1)I_1 + a^2 \cdot I_2] + (\delta_{ik} \cdot \delta_{j\ell} + \delta_{jk} \\ & \cdot \delta_{i\ell})[(1 - 2\nu^0)I_1 + a^2 \cdot I_2] + [2\nu^0 \cdot \delta_{k\ell} \cdot x_i \\ & + (1-\nu^0)(\delta_{i\ell} \cdot x_k + \delta_{ik} \cdot x_\ell)]I_{1,j} + (1-\nu^0) \\ & \times [\delta_{j\ell} \cdot x_k + \delta_{jk} \cdot x_\ell]I_{1,i} - [\delta_{ij} \cdot x_k + \delta_{ik} \cdot x_j + \delta_{jk} \\ & \cdot x_i](I_{1,\ell} - a^2 \cdot I_{2,\ell}) - [\delta_{i\ell} \cdot x_j + \delta_{j\ell} \cdot x_i](I_{1,k} - a^2 \\ & \cdot I_{2,k}) - x_i \cdot x_j(I_{1,\ell k} - a^2 \cdot I_{2,\ell k}) \end{aligned} \tag{20}$$

In Eq. (20), the symbol δ_{ij} designates the Kronecker symbol, and the functions I_1 and I_2 are defined by:

$$I_1(\vec{x}) = \frac{4\pi a^3}{3\|\vec{x}\|^3},\quad I_2(\vec{x}) = \frac{4\pi a^3}{5\|\vec{x}\|^5} \tag{21}$$

At last, partial derivatives of I_1 and I_2 are given by:

$$\begin{aligned} I_{1,i} &\equiv \frac{\partial I_1}{\partial x_i} = -4\pi a^3 \|\vec{x}\|^{-5} x_i, \\ I_{1,ij} &\equiv \frac{\partial^2 I_1}{\partial x_i \partial x_j} = -4\pi a^3 \|\vec{x}\|^{-5} (\delta_{ij} - 5\|\vec{x}\|^{-2} x_i \cdot x_j) \\ I_{2,i} &\equiv \frac{\partial I_2}{\partial x_i} = -4\pi a^3 \|\vec{x}\|^{-7} x_i, \\ I_{2,ij} &\equiv \frac{\partial^2 I_2}{\partial x_i \partial x_j} = -4\pi a^3 \|\vec{x}\|^{-7} (\delta_{ij} - 7\|\vec{x}\|^{-2} x_i \cdot x_j) \end{aligned} \tag{22}$$

It is to be noted that Eq. (19), with $\overline{\overline{\overline{D}}}(\vec{x})$ defined by Eqs. (20)–(22), holds both for exterior points and interior points. Indeed, as shown in e.g. Mura's work [43], for interior points, $I_1 = \frac{4\pi}{3}$ and $I_2 = \frac{4\pi}{5a^2}$ and their partial derivatives vanish in Eq. (20). Therefore, $\overline{\overline{\overline{D}}}(\vec{x}) = \overline{\overline{\overline{S}}}$ and Eq. (19) becomes equivalent to Eq. (15).

In conclusion, for a spherical inhomogeneity I in an infinitely extended isotropic elastic material subjected to $\overline{\overline{\varepsilon}}^0$ at infinity, the strain tensor $\overline{\overline{\varepsilon}}^I$ in I is calculated by Eq. (15) with $\overline{\overline{\varepsilon}}^*$ given by Eq. (16), (or equivalently by Eq. (17)), with $\overline{\overline{\overline{S}}}$ given by Eq. (18). The strain tensor in the matrix $\overline{\overline{\varepsilon}}(\vec{x})$ is calculated by Eq. (19) with $\overline{\overline{\overline{D}}}(\vec{x})$ given by Eqs. (20)–(22). The stress tensors inside and outside the inhomogeneity are derived from the elastic laws:

$$\begin{cases} \overline{\overline{\sigma}}^I = \overline{\overline{\overline{C}}}^I : \overline{\overline{\varepsilon}}^I \\ \overline{\overline{\sigma}}(\vec{x}) = \overline{\overline{\overline{C}}}^0 : \overline{\overline{\varepsilon}}(\vec{x}) \end{cases} \tag{23}$$

The above mentioned expressions are valid in the general case of a spherical defect regardless of its nature. In the special case of a spherical cavity (pore) discussed in the following section, elastic moduli are equal to zero ($\overline{\overline{\overline{C}}}^I = \overline{\overline{\overline{0}}}$).

4.3. Identification of the parameters of DSG criterion

According to the Basquin's law, we can obtain the fatigue strengths in tension at the number of cycles $N = 5 \times 10^6$ for both load ratios: $\sigma^{te}_{D-1} = 91$ MPa, $\sigma^{te}_{D0.1} = 66$ MPa.

According to the DSG criterion, we obtain:

$$\begin{cases} \dfrac{\sigma^{te}_{D-1}}{\sqrt{3}} + \alpha \cdot \dfrac{\sigma^{te}_{D-1}}{3} = \beta \\ \dfrac{\sigma^{te}_{D0.1}}{\sqrt{3}} + \alpha \cdot \dfrac{2}{1-0.1} \cdot \dfrac{\sigma^{te}_{D0.1}}{3} = \beta \end{cases} \tag{24}$$

So α and β can be identified. As the fatigue strength for the load ratios $R = -1$ and 0.1 are obtained for a number of cycles $N = 5 \times 10^6$, the constants α and β are calculated as the values at this number of cycles.

The identification of the third parameter b needs to know the fatigue strength for a given defect. The DSG criterion (Eq. (4)) can be transformed into:

$$b = \frac{\sqrt{area}(\sigma_{eq,max} - \beta)}{\sigma_{eq,max} - \sigma^{\infty}_{eq}} \tag{25}$$

In order to evaluate $\sigma_{eq,max}$, for a tensile stress with the only non-zero component applied far from the defect σ^{∞}_{11}, the stress tensor at the most loaded point on the spherical void surface is calculated analytically using the Eshelby's theory:

$$\overline{\overline{\sigma}}_{loc,max} = \sigma^{\infty}_{11} \begin{pmatrix} 2.05 & 0 & 0 \\ 0 & 0.136 & 0 \\ 0 & 0 & 0 \end{pmatrix} \tag{26}$$

In this study, a defect size $\sqrt{area} = 723$ μm corresponding to a fatigue strength $\sigma_a = 45$ MPa with a load ratio $R = 0.1$ is used to identify b.

The identified values of the three parameters are: $\alpha = 0.801$, $\beta = 76.8$ MPa, $b = 540$ μm.

4.4. Simulation of Kitagawa diagram

Once the parameters α, β and b identified, we can simulate the Kitagawa diagram for tension loading using DSG criterion and Eq. (26). Considering that a small defect has no influence on the fatigue strength, the criterion can be defined as below:

$$\begin{cases} \sigma^*_{eq} = \sigma_{CR,max} - b \cdot \dfrac{\sigma_{CR,max} - \sigma^{\infty}_{CR}}{\sqrt{area}} \quad if \quad \sigma^*_{eq} < \beta \\ \sigma^*_{eq} = \sigma_D \quad if \quad \sigma^*_{eq} \geqslant \beta \end{cases} \tag{27}$$

It can be seen in Figs. 16 and 17 that the DSG criterion can describe correctly the influence of defect on fatigue strength for both load ratios. For most specimens with no defect or small defects, the simulated curve goes through failure and non failure stress levels. For big defects and a load ratio $R = 0.1$, the simulated curve traverses failure and non failure stress levels or lies slightly above failure stress levels or near last non failure stress levels. However, the DSG criterion overestimates the dropping rate of the fatigue strength with the defect size and the critical defect size showing influence on the fatigue strength. The simulation for $R = 0.1$ is not as good as that for the load ratio $R = -1$ in the big-defect-size zone. The DSG criterion underestimates the fatigue strength. The local

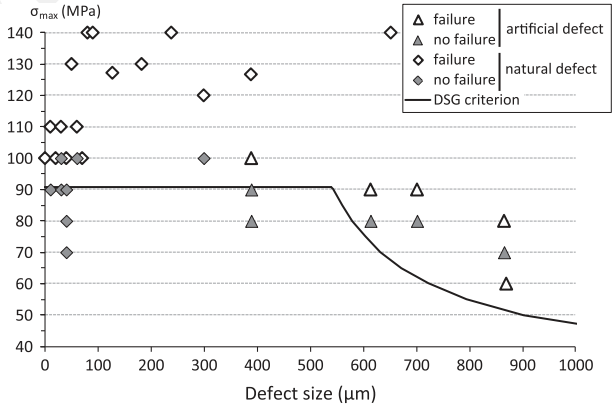

Fig. 16. Simulation of Kitagawa diagram using DSG criterion. Tension loading, $R = -1$.

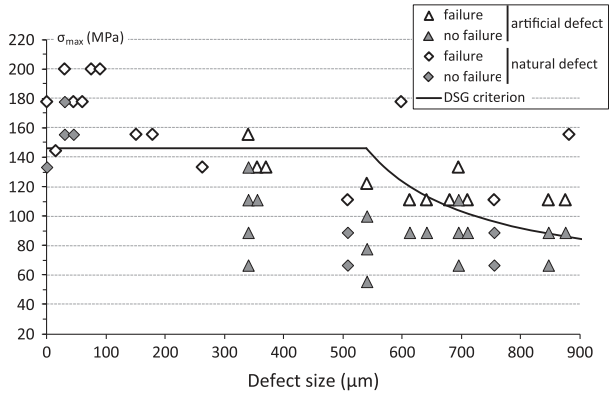

Fig. 17. Simulation of Kitagawa diagram using DSG criterion. Tension loading, $R = 0.1$.

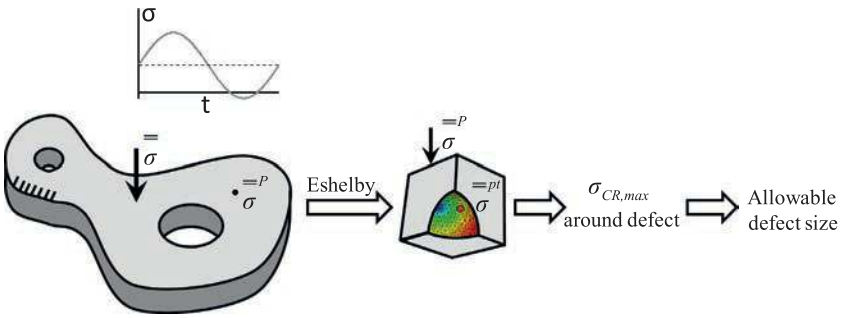

Fig. 18. Simulation procedure using DSG criterion.

plasticity around the defect that is not taken into account in the simulation explains probably this result. Indeed, it can be shown thanks to the Eshelby's method (Eq. (26) notably) that the maximum von Mises equivalent stress on a spherical defect surface exceeds the material yield strength (275 MPa) when the tensile stress applied far from the defect is larger than 134 MPa.

4.5. Finite element simulation on industrial component

The DSG approach with Eshelby submodel has been implemented as an UVARM – subroutine for ABAQUS®. An UVARM allows creating user-defined output variables at the integration points of a finite element model. The calculation procedure with UVARM is shown in Fig. 18. The FE simulation of the component is here performed considering the material isotropic linear elastic and may be done with any periodic proportional cyclic loading. The methodology is the following. First, the modeling and the meshing of the considered component are done and the boundary conditions and loads prescribed in ABAQUS®. Then, the macroscopic FE simulation of the component is performed. Thanks to the UVARM subroutine, the stress tensor at each point P of the component, $\overline{\overline{\sigma}}^{P}$, is extracted and used as input for the DSG approach. $\overline{\overline{\sigma}}^{P}$ is applied at infinity (i.e. far from the defect) in the Eshelby submodel. The latter allows the computation of the stresses at each point on the defect surface $\overline{\overline{\sigma}}^{pt}$ (side matrix). By comparing σ_{CR}^{pt} of all points on the defect surface, the maximum Crossland equivalent stress $\sigma_{CR,\max}$ is obtained. Together with the infinite Crossland equivalent stress at point P, σ_{CR}^{∞}, the allowable defect size according to this loading condition is determined using DSG criterion.

A crank model with a hole at each end (Fig. 19) has been considered as a first example in order to illustrate the feasibility of the DSG approach application to a structure. The angle between the straight line connecting the centers of two holes in the Y–Z plane and the Z-axis (Fig. 19) is equal to 11.5°. The encastre boundary condition has been applied to the inner surface of the big hole. A surface traction load along the Z-axis has been prescribed on the inner surface of the small hole. The stress is sinusoidal and the load ratio is −1. A loading period of 1 s with 4 increments has been considered. The model has been meshed with quadratic tetrahedron elements (C3D10) with size equal to 2 mm. The computation time for the chosen element size and loading increments was 30 min.

Fig. 19. Allowable defect size distribution on the crank model.

Fig. 19 illustrates the distribution of the allowable defect size using DSG criterion. The zones with a defect size between 300 and 1000 μm are separated by different colors. It has been observed that the allowable defect size is generally small in regions with high Crossland equivalent stress. This means that more attention should be paid in these regions during fabrication.

The UVARM based on the DSG criterion is a convenient visual tool in the industrial fabrication quality control. The size of defect found in an industrial component can be measured and then compared to that at the same position in the model simulated under the expected loading conditions and fatigue life. If the defect size exceeds the allowable size, the component will not be safe to use.

5. Conclusion

Tension fatigue tests with load ratios $R = -1$ and 0.1 have been performed on AS7G06-T6 alloy. The "step loading" procedure was used to evaluate the fatigue strength. Both defect-free specimens and those with natural or artificial defects (size between 100 and 900 μm) have been tested. The Basquin's law has been used to moderate the Wöhler curves.

- The mean stress effect is analyzed and results show that this effect can be described by the Goodman approach.
- Several crack initiation sites have been found on fracture surface: crystallographic initiation without defect, shrinkage cavity and oxidized skin. The parameter $\sqrt{area}$ is adopted to measure the defect size. In order to produce additional results for big defect sizes, artificial defects have been fabricated using spark erosion machining. Kitagawa diagrams show that a defect influences the fatigue strength when its size is larger than 300 ± 100 μm. This value is of the same order of magnitude than the grain size (259–573 μm), and higher than the SDAS (38 μm).
- The DSG approach is adopted to simulate the defect influence on the fatigue strength. The Eshelby's method is used to calculate the stress around the defect. The DSG approach gives relatively good results to simulate Kitagawa diagrams in tension loading for two load ratios $R = -1$ and 0.1.
- The DSG approach, including Eshelby submodel for a spherical pore, has been implemented as an UVARM- subroutine in ABAQUS®. This tool allows the post-treatment of the FE simulation of a real, industrial, component. It provides the distribution of the allowable defect size on the structure, and is thus conve-

nient in the industrial quality control as well as in the fatigue design process of casting parts. A crank model has been chosen for a first illustration of the methodology.

The DSG criterion needs to be improved for better description of the Kitagawa diagram. The influence of acuity of the defect will be considered to analyze the case of nonspherical defects. Furthermore, more realistic local stress fields will be obtained by computing the fatigue behavior of cast products in consideration of plastic deformation near the defect.

Acknowledgements

This work is part of the IDEFFAAR (Influence des DEfauts de Fonderie sur la Fatigue des Alliages Aéronautiques) project, which is financed by ANR (National Research Agency, through Grant ANR-2010-RMNP-016-01). The authors also wish to thank Jean-Yves Buffière from INSA Lyon, and also Fonderie Messier, SAFRAN and AIRBUS for their contribution to the IDEFFAAR project.

References

[1] Murakami Y. Stress concentration. In: Murakami Y, editor. Metal fatigue: effects of small defects and nonmetallic inclusions. Oxford: Elsevier; 2002. p. 11–24.
[2] Murakami Y, Endo M. Effects of defects, inclusions and inhomogeneities on fatigue strength. Int J Fatigue 1994;16:163–82.
[3] Vallellano C, Mariscal MR, Navarro A, Dominguez J. A micromechanical approach to fatigue in small notches. Fat Frac Eng Mater Struct 2005;28:1035–45.
[4] Owolabi G, Prasannavenkatesan R, McDowell D. Probabilistic framework for a microstructuresensitive fatigue notch factor. Int J Fatigue 2010;32:1378–88.
[5] Buffière J-Y, Savelli S, Jouneau PH, Maire E, Fougères R. Experimental study of porosity and its relation to fatigue mechanisms of model Al–Si7–Mg0.3 cast Al alloys. Mater Sci Eng A 2001;316:115–26.
[6] Nicoletto G, Anzelotti G, Konečná R. X-ray computed tomography vs. metallography for pore sizing and fatigue of cast Al-alloys. Procedia Eng 2010;2:547–54.
[7] Susmel L, Taylor D. Two methods for predicting the multiaxial fatigue limits of sharp notches. Fat Frac Eng Mater Struct 2003;26:821–33.
[8] Leopold G, Nadot Y. Fatigue from an induced defect: experiments and application of different multiaxial fatigue approaches. J ASTM Int 2010:7.
[9] Thieulot-Laure E, Pommier S, Fréchinet S. A multiaxial fatigue failure criterion considering the effects of the defects. Int J Fatigue 2007;29:1996–2004.
[10] Kitagawa H, Takahashi S. Applicability of fracture mechanics to very small cracks or the cracks in the early stages. In: Proceedings of the second international conference on mechanical behavior of materials, Boston; 1976. p. 627–31.
[11] Beretta S, Foletti S, Valiullin K. Fatigue strength for small shallow defects/cracks in torsion. Int J Fatigue 2011;33:287–99.
[12] Billaudeau T, Nadot Y, Bezine G. Multiaxial fatigue limit for defective materials: mechanisms and experiments. Acta Mater 2004;52:3911–20.
[13] Nadot Y, Billaudeau T. Multiaxial fatigue limit criterion for defective materials. Eng Fract Mech 2006;73:112–33.
[14] Papadopoulos IV. Invariant formulation of a gradient dependent multiaxial high-cycle fatigue criterion. Eng Fract Mech 1996:513–28.
[15] Morel F, Morel A, Nadot Y. Comparison between defects and micro-notches in multiaxial fatigue – the size effect and the gradient effect. Int J Fatigue 2009;31:263–75.
[16] Gadouini H, Nadot Y, Rebours C. Influence of mean stress on the multiaxial fatigue behaviour of defective materials. Int J Fatigue 2008;30:1623–33.
[17] Roy MJ, Nadot Y, Nadot-Martin C, Bardin PG, Maijer DM. Multiaxial Kitagawa analysis of A356-T6. Int J Fatigue 2011;33:823–32.
[18] Miller KJ. The behaviour of short fatigue cracks and their initiation – Part I: a review of two recent. Fat Frac Eng Mater Struct 1987;10:75–91.
[19] Miller KJ. The behaviour of short fatigue cracks and their initiation – Part II: a general summary. Fat Frac Eng Mater Struct 1987;10:93–113.
[20] ASTM International, E155-05: Standard Reference Radiographs for Inspection of Aluminum and Magnesium Castings. West Conshohocken; 2005.
[21] Bellows RS, Muju S, Nicholas T. Validation of the step test method for generating Haigh diagrams for Ti–6Al–4V. Int J Fatigue 1999;21:687–97.
[22] Murakami Y, Tazunoki Y, Endo T. Existence of the coaxing effect and effects of small artificial holes on fatigue strength of an aluminum alloy and 70–30 brass. Metall Mater Trans A 1984;15:2029–38.
[23] Yi JZ, Gao YX, Lee PD, Flower HM, Lindley TC. Scatter in fatigue life due to effects of porosity in cast A356-T6 aluminum–silicon alloys. Metall Mater Trans A 2003;34:1879–90.
[24] Jana S, Mishra RS, Baumann JB, Grant G. Effect of friction stir processing on fatigue behavior of an investment cast Al–7Si–0.6 Mg alloy. Acta Mater 2010;58:989–1003.
[25] Wang QG, Apelian D, Lados DA. Fatigue behavior of A356-T6 aluminum cast alloys. Part I. Effect of casting defects. J Light Met 2001;1:73–84.
[26] Brochu M, Verreman Y, Ajersch F, Bouchard D. High cycle fatigue strength of permanent mold and rheocast aluminum 357 alloy. Int J Fatigue 2010;32:1233–42.
[27] Brochu M, Verreman Y, Ajersch F, Bouchard D. Propagation of short fatigue cracks in permanent and semi-solid mold 357 luminum alloy. Int J Fatigue 2012;36:120–9.
[28] Koutiri I, Bellett D, Morel F, Augustins L, Adrien J. High cycle fatigue damage mechanisms in cast aluminium subject to complex loads. Int J Fatigue 2013;47:44–57.
[29] Koutiri I, Bellett D, Morel F, Pessard E. A probabilistic model for the high cycle fatigue behaviour of cast aluminium alloys subject to complex loads. Int J Fatigue 2013;47:137–47.
[30] Sonsino CM, Grubisic V. Requirements for operational fatigue strength of high quality cast components. Materialwiss Werkstofftech 1996;27:373–90.
[31] Crossland B. Effect of large hydrostatic pressures on the torsional fatigue strength of fan alloy steel. In: Proceedings of the international conference on fatigue of metals. London and New York; 1956. p. 138–49.
[32] Yi JZ, Gao YX, Lee PD, Flower HM, Lindley TC. Scatter in fatigue life due to effects of porosity in cast A356-T6 aluminum–silicon alloys. Mater Trans A 2003;34:1879–90.
[33] Li P, Lee PD, Maijer DM, Lindley TC. Quantification of the interaction within defect populations on fatigue behavior in an aluminum alloy. Acta Mater 2009;57:3539–48.
[34] Luo Z, Zhong E. Derivation of formula for any polygonal area and its applications. College Math 2005;21:123–5.
[35] Murakami Y. Effect of hardness Hv on fatigue limits of materials containing defects, and fatigue limit prediction equations. In: Murakami Y, editor. Metal fatigue: effects of small defects and nonmetallic inclusions. Oxford: Elsevier; 2002. p. 57–71.
[36] Dang Van K, Griveau B, Message O. On a new multiaxial fatigue limit criterion: theory and applications, biaxial and multiaxial fatigue. In: Brown MW, Miller KJ, editors. EGF 3. London: Mechanical Engineering Publications; 1989. p. 479–96.
[37] Vu QH, Halm D, Nadot Y. Multiaxial fatigue criterion for complex loading based on stress invariants. Int J Fatigue 2010;32:1004–14.
[38] Karolczuk A, Nadot Y, Dragon A. Non-local stress gradient approach for multiaxial fatigue of defective material. Comput Mater Sci 2008;44:464–75.
[39] Ben Sghaier R, Bouraoui Ch, Fathallah R, Hassine T, Dogui A. Probabilistic high cycle fatigue behaviour prediction based on global approach criteria. Int J Fatigue 2007;29:209–21.
[40] Eshelby JD. The determination of the elastic field of an ellipsoidal inclusion, and related problems. Proc R Soc Lond A 1957;241:376–96.
[41] Eshelby JD. Elastic inclusions and inhomogeneities. In: Sneddon IN, Hill R, editors. Progress in solid mechanics 2. Amsterdam: North-Holland Publishing Company; 1961. p. 89–140.
[42] Hill R. Continuum micro-mechanics of elastoplastic polycrystals. J Mech Phys Sol 1965;13:89–101.
[43] Mura T. Micromechanics of defects in solids. Mechanics of elastic and inelastic solids. In: Nemat-Nasser S, Oravas GAE, editors. Martinus Nijhoff Publishers; 1987.